

and detector scatter responses can be partially inscribed in the models using singular-value decomposition (11) or piecewise Fourier inversion (12). Second, the presence of the geometric component in the inverse requires a low-pass filter to suppress noise at high frequency. To overcome this limitation, a tradeoff between noise amplification and resolution loss can be made by setting the geometric component in the inverse filter to a constant value equal to its intensity. This enables one to omit the low-pass filter, since the inverse converges to this value at high frequency. In so doing, the scatter-corrected projections, unrestored for the intrinsic detector resolution, become in the different models:

$$\text{DR: } P_{\text{od}} = P_{\text{m}} / \{f_{\text{g}} + H_{\text{d}} + H_{\text{o}}\} \quad \text{Eq. 15a}$$

$$\text{DS: } P'_{\text{od}} = P_{\text{m}} / \left\{ 1 + \frac{H_{\text{d}} + H_{\text{o}}}{f_{\text{g}}} \right\} \quad \text{Eq. 15b}$$

$$\text{DSR: } P''_{\text{od}} = P_{\text{m}} / \left\{ \frac{f_{\text{g}} + H_{\text{d}} + H_{\text{o}}}{f_{\text{g}} + f_{\text{d}}} \right\} \quad \text{Eq. 15c}$$

When the detector scatter intensity is small, such as is the case for lower resolution PET systems, both the DS and DSR models become identical and reduce to the gener-

alized scatter correction method commonly used in single photon emission tomography (9). When the detector scatter spread is narrow, a low-pass filter may still be required in the DR and DSR models since the inverse converges to a constant value above unity at high frequency. The inclusion of detector scatter in the desired components for image formation (2) suggests that some fraction of the object scatter which may not be detrimental to image quality could, in principle, be included as well. Such a model would undoubtedly reconcile the imaging goals of both *reformists* and *purists* in nuclear medicine.

REFERENCES

1. Links JM. Scattered photons as "good counts gone bad": are they reformable or should they be permanently removed from society? *J Nucl Med* 1995;36:130-132.
2. Bentourkia M, Msaki P, Cadorette J, Lecomte R. Assessment of scatter components in high resolution PET: correction by nonstationary convolution subtraction. *J Nucl Med* 1995;35:121-130.
3. Bentourkia M, Msaki P, Cadorette J, Lecomte R. Energy dependence of scatter components in multispectral PET imaging. *IEEE Trans Med Imag* 1995;14:138-145.
4. Thompson CJ, Picard Y. Two new strategies to increase the signal to noise ratio in positron volume imaging. *IEEE Trans Nucl Sci* 1993;40:956-961.
5. Links JM, Leal JP, Mueller-Gaertner HW, Wagner

HN. Improved positron emission tomography quantification by Fourier-based restoration filtering. *Eur J Nucl Med* 1992;19:925-932.

6. King MA, Coleman M, Penney BC, Glick SJ. Activity quantitation in SPECT: a study of prereconstruction Metz filtering and the use of the scatter degradation factor. *Med Phys* 1991;18:184-189.
7. Frey EC, Tsui BMW. A practical method for incorporating scatter in a projector-backprojector for accurate scatter compensation in SPECT. *IEEE Trans Nucl Sci* 1993;40:1107-1116.
8. Bergström M, Eriksson L, Bohm C, Blomqvist G, Litton J. Correction for scattered radiation in a ring detector positron camera by integral transformation of the projections. *J Comput Assist Tomogr* 1983;7:42-50.
9. Msaki P, Axelsson B, Dahl CM, Larsson SA. A generalized scatter correction method in SPECT using point scatter distribution functions. *J Nucl Med* 1987;28:1861-1869.
10. Msaki P, Erlandsson K, Svensson L, Nilstedt L. The convolution scatter subtraction hypothesis and its validity domain in radioisotope imaging. *Phys Med Biol* 1993;38:1359-1370.
11. Lewitt RM, Muehllehner G, Karp J. Three-dimensional image reconstruction for PET by multi-slice rebinning and axial image filtering. *Phys Med Biol* 1994;39:321-339.
12. Bentourkia M, Msaki P, Cadorette J, Lecomte R. Nonstationary scatter subtraction-restoration in high resolution PET. *J Nucl Med* 1996;37:2040-2046.

P. Msaki

M. Bentourkia

R. Lecomte

University of Sherbrooke
Sherbrooke, Quebec, Canada

A Graphical Analysis Method to Estimate Blood-to-Tissue Transfer Constants for Tracers with Labeled Metabolites

David A. Mankoff, Anthony F. Shields, Michael M. Graham, Jeanne M. Link and Kenneth A. Krohn

Division of Nuclear Medicine, University of Washington, Seattle, Washington; Wayne State University and the Karmanos Cancer Institute, Detroit, Michigan

The Patlak graphical analysis technique is a popular tool for estimating blood-to-tissue transfer constants from multiple-time uptake data. Our objective was to extend this technique to tracers with labeled metabolites, the presence of which can cause errors in the standard Patlak analysis. **Methods:** Based on previously described formulations, we generalized the graphical technique for use under specific conditions. To test the extended graphical approach, we applied the method to both simulated and patient data using a preliminary compartmental model for the PET tumor proliferation marker, 2-[¹¹C]-thymidine. **Results:** When given conditions are met, a linear relationship exists between the normalized tissue activity (tissue activity/blood activity) and a new set of graphical analysis basis functions, including a new definition of normalized time, which takes the presence of labeled metabolites into account. Graphical estimations of the tumor thymidine incorporation rate for simulated data were accurate and showed close agreement to the results of detailed compartmental analysis. In patient studies, the graphical

and compartmental estimates showed good agreement but a somewhat poorer correlation than in the simulations. **Conclusion:** The extended graphical analysis approach provides an efficient method for estimating blood-tissue transfer constants for tracers with labeled metabolites.

Key Words: PET; modeling; carbon-11-thymidine; metabolites

J Nucl Med 1996; 37:2049-2057

Radiopharmaceutical imaging is frequently complicated by the presence of labeled metabolites. The metabolites usually have a different distribution pattern than the parent tracer and can therefore cause errors in the kinetic analysis. When the blood concentrations of the tracer and its metabolites are known through blood sampling and metabolite analysis, tracer kinetic modeling can be used to separate the contributions of tracer and metabolites to the image and to estimate physiologic parameters based upon the tracer of interest. Models accounting for the behavior of the intact tracer and its metabolites are, by necessity, more complex and generally ill-suited for the routine estimation of physiologic parameters. In general, only the

Received May 22, 1995; revision accepted Feb. 28, 1996.

For correspondence or reprints contact: David A. Mankoff, MD, PhD, Division of Nuclear Medicine, Box 356113, University of Washington Medical Center, 1959 NE Pacific St., Seattle, WA 98195.

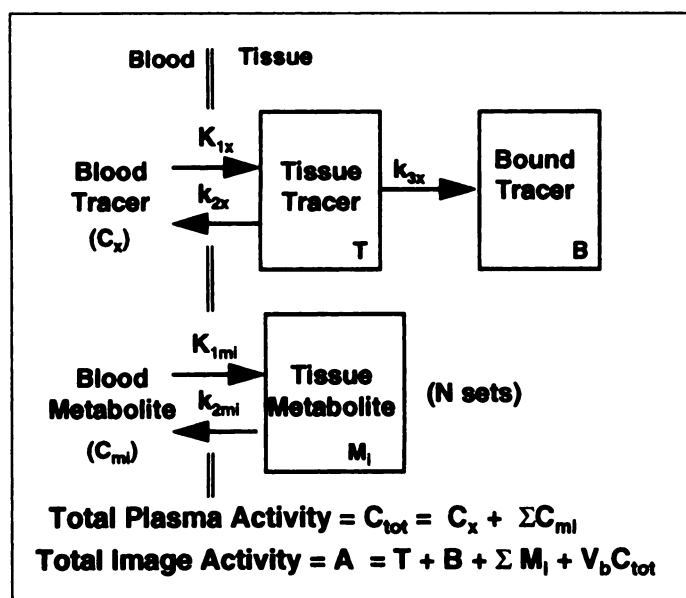


FIGURE 1. Graphical analysis for systems with labeled metabolites, irreversible trapping of intact tracer and no irreversible trapping of the metabolites.

parameters pertaining to the parent tracer are of interest. However, to avoid bias, one must also estimate kinetic parameters for each class of labeled metabolites. Therefore, a method capable of simplifying the quantitative analysis of metabolized tracers without ignoring the contribution of labeled metabolites would be desirable.

The graphical analysis method of Patlak (1,2) and Gjedde (3) has been applied to tracers which are irreversibly or effectively irreversibly trapped in tissue. This can include either metabolic trapping in the case of [^{18}F]fluorodeoxyglucose (4–6), or receptor binding, as in the case of receptor agonists with slow off rates. In such situations, a transformation of the data leads to a simple graphical relationship that can be used to estimate the steady-state flux of the traced substance from the blood to tissue. Martin et al. (7) described a graphical method used to estimate the flux of [^{18}F]FDOPA into the striatal cortex that corrects for labeled metabolites using the measured activity from a region of the brain that does not trap FDOPA. While such methods are appropriate for brain studies, in tumor imaging no appropriate tissue for metabolite correction is available. Patlak et al. (8) described a reformulation of the graphical method for FDOPA imaging that does not require tissue subtraction. Willemsen et al. (9) presented a similar methodology to estimate the incorporation of [C-11]tyrosine, but it required a period of time when the level of labeled metabolites remained a constant fraction of total blood activity.

We present a general extension of Patlak's formulation applicable to systems with multiple metabolites under the condition that none of the labeled metabolites is irreversibly trapped in the tissue of interest. Examples of tracers (with metabolites) to which this method is potentially applicable include 2-[^{11}C]thymidine (thymine, CO_2) (10,11), [^{18}F]FDOPA (3-OMFD) (7,12) and 1-[^{11}C]tyrosine (L-DOPA, CO_2) (9). We present a theoretical background for our method and test its application to the tumor imaging agent, 2-[^{11}C]thymidine, using both simulated and patient data. The results shown for both simulated and patient data are not a validation of the model, but only a test of the ability of the graphical method to estimate tracer blood-tissue transfer constants under practical imaging conditions.

Mathematical Development

Review of Graphical Analysis. Although the original description by Patlak et al. (1) allows the graphical method to be applied to more complex models, we will confine ourselves to the simple compartmental model illustrated in the first compartment set in Figure 1, subscript x. In the original formulation, the following assumptions were made:

1. Both the blood and tissue tracer concentrations over time are known. The blood is the only source of the tracer.
2. Tracer kinetics can be described by an exchangeable tissue compartment plus a single compartment into which there is unidirectional flux (i.e., trapping). Labeled metabolites in the blood or reversible tissue compartment behaving differently from the intact tracer are not allowed, and any labeled metabolites generated in the tissue must remain trapped in the irreversible compartment.
3. The system obeys first order kinetics for transfer between compartments.
4. There exists a time, t^* , when the system reaches a quasi steady-state, and the exchangeable compartment is in near equilibrium with the blood. After t^* , the time constant for the change in the plasma tracer concentration is much less than the rate constant for efflux from the exchangeable compartment. Using the parameter names illustrated in Figure 1, this is equivalent to the following:

for $t > t^*$

$$\frac{dC_x/dt}{C_x} \ll k_{2x} + k_{3x}, \quad \text{Eq. 1}$$

where C_x is the time-varying blood concentration of the tracer and k_{2x} and k_{3x} are rate constants illustrated in the first compartment set in Figure 1. Under these conditions, a transformation of the data (1–3) will result in a relationship which is linear after t^* :

$$\frac{A}{C_x} = K_x \frac{\int C_x d\tau}{C_x} + (V_{0x} + V_b), \quad \text{Eq. 2}$$

where A is the time-varying tissue tracer activity (obtained from dynamic imaging), K_x is the tracer blood-tissue transfer constant, V_b is the blood volume per unit tissue, and V_{0x} is the volume of distribution for the tracer. The blood-tissue transfer constant, K_x , is usually the parameter of interest, and the steady-state flux of the traced substance from the blood into the bound compartment can be calculated as follows:

$$\text{Flux} = K_x [X], \quad \text{Eq. 3}$$

where $[X]$ is the blood concentration of the native substance (not the tracer) and is assumed to be constant over the time that the system is observed. For the model illustrated in Figure 1, in keeping with the model of Sokoloff et al. (4), K_x is given by the following:

$$K_x = \frac{K_{1x}k_{3x}}{k_{2x} + k_{3x}}. \quad \text{Eq. 4}$$

According to Equation 2, K_x is the slope of the line A/C_x compared with $\int C_x d\tau / C_x$. We refer to the first quantity as the normalized tissue activity and the latter as the normalized or extended time.

Extension to Systems with Labeled Metabolites. In the application to tracers with labeled metabolites, we make all of the assumptions listed above for the parent tracer (subscript x), except that we now allow the presence of labeled metabolites

(subscript m_i) in the blood that behave differently from the tracer. The following additional assumptions are made:

1. The blood concentrations of the tracer and its metabolites are known over time. Only the sum of the tissue concentrations of the tracer and its metabolites is known.
2. The blood is the source of metabolites for the tissue of interest; i.e., a tissue other than the tissue of interest is principally responsible for the generation of metabolites.
3. The metabolites undergo only reversible exchange between blood and tissue; none of the metabolites is irreversibly trapped.
4. There exists a time, t^* , after injection when each compartment set reaches quasi steady-state. In addition to the condition specified by Equation 1, we also require for each metabolite compartment set, i :

$$\frac{dC_{mi}/dt}{C_{mi}} \ll k_{2mi} \quad \text{for all } i. \quad \text{Eq. 5}$$

Under these conditions, the following holds for the intact tracer:

$$\frac{A_x}{C_x} = K_x \frac{\int C_x d\tau}{C_x} + (V_{0x} + V_b), \quad \text{Eq. 6}$$

where A_x is the portion of tissue activity attributable to the intact tracer.

For the i^{th} metabolite, since there is no irreversible trapping, k_{3mi} is zero, and thus K_{mi} is zero. Therefore, the following simple relationship holds:

$$\frac{A_{mi}}{C_{mi}} = V_{0mi} + V_b, \quad \text{Eq. 7}$$

where A_{mi} is the portion of the tissue activity arising from the i^{th} metabolite, and V_{0mi} is the distribution volume for the i^{th} metabolite. Adding Equation 6 and Equation 7 for each metabolite and rearranging terms result in the following:

$$\frac{A}{C_{\text{tot}}} = K_x \frac{\int C_x d\tau}{C_{\text{tot}}} + V_{0x} \frac{C_x}{C_{\text{tot}}} + \sum V_{0mi} \frac{C_{mi}}{C_{\text{tot}}} + V_b, \quad \text{Eq. 8}$$

where A is the total tissue activity $= A_x + \sum A_{mi}$ and C_{tot} is the total blood activity $= C_x + \sum C_{mi}$. Equation 8 describes a relationship between the normalized tissue activity and a linear combination of basis functions: $\int C_x d\tau / C_{\text{tot}}$, C_x / C_{tot} , several C_{mi} / C_{tot} , and 1, with a set of parameters: K_x (tracer blood-tissue transfer constant and parameter of interest), V_{0x} , several V_{0mi} , and V_b . This allows estimation of the tracer blood-tissue transfer constant using linear estimation methods with a reduced number of parameters.

Special Cases. In general, we are most interested in K_x and less interested in the individual volume terms in Equation 8. Under the condition that there is a single dominant metabolite (referred to as Special Case I), Equation 8 can be rewritten as follows:

$$\frac{A}{C_{\text{tot}}} = K_x \frac{\int C_x d\tau}{C_{\text{tot}}} + V_1 \frac{C_m}{C_{\text{tot}}} + V_2, \quad \text{Eq. 9}$$

where the subscript m refers to the dominant metabolite and

$$V_1 = V_{0m} - V_{0x} \quad \text{Eq. 10}$$

$$V_2 = V_b + V_{0x}. \quad \text{Eq. 11}$$

This is the form proposed by Patlak et al. (8) for FDOPA. In this case, only three parameters need to be estimated, K_x , V_1 and V_2 .

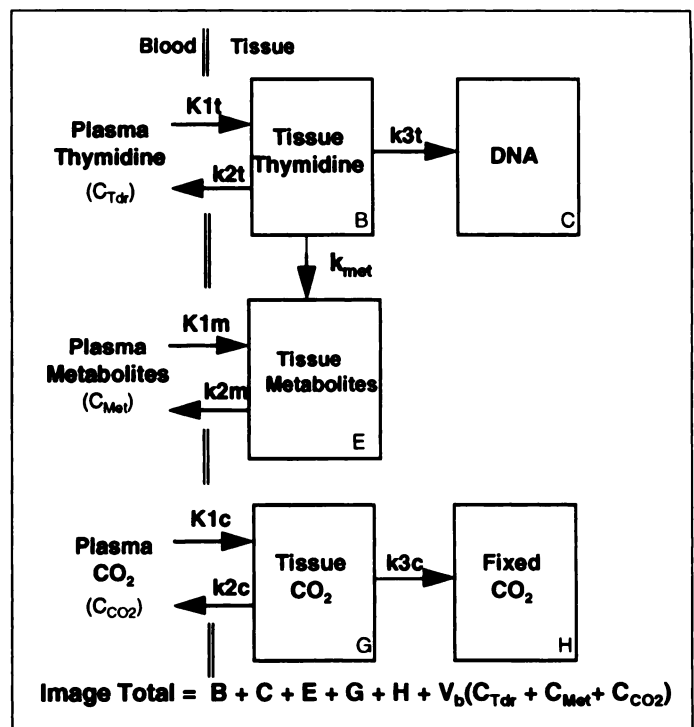


FIGURE 2. Compartmental model for 2-[^{11}C]-thymidine behavior in vivo. Line in the third compartment set (CO_2) indicates the possibility of CO_2 trapping in tissue. The line connecting the tissue thymidine and metabolite compartments indicates the degradation pathway used in simulations of local tissue metabolism of thymidine.

Under the condition that the tracer and its metabolites reach constant relative activities in the blood after time, t^* , further simplifications are possible (referred to as Special Case II). Under these conditions:

$$\frac{A}{C_{\text{tot}}} = K_x \frac{\int C_x d\tau}{C_{\text{tot}}} + V, \quad \text{Eq. 12}$$

where

$$V = V_{0x} \frac{C_x}{C_{\text{tot}}} + \sum V_{0mi} \frac{C_{mi}}{C_{\text{tot}}} + V_b, \quad \text{Eq. 13}$$

which is a constant by virtue of the fact that C_x / C_{tot} and all the C_{mi} / C_{tot} are all constant for $t > t^*$. The estimation of K_x is reduced to a simple linear fit as in conventional Patlak analysis. This relationship looks very similar to the original Patlak relationship, except for the new definition of normalized time that takes the presence of labeled metabolites into account.

Metabolite Trapping. We also consider the case in which one of the metabolites, denoted by subscript m^* , undergoes irreversible trapping in the tissue. In this situation, the following equation applies:

$$\frac{A}{C_{\text{tot}}} = K_x \frac{\int C_x d\tau}{C_{\text{tot}}} + V_{0x} \frac{C_x}{C_{\text{tot}}} + \sum V_{0mi} \frac{C_{mi}}{C_{\text{tot}}} + V_b + K_{m^*} \frac{\int C_{m^*} d\tau}{C_{\text{tot}}}, \quad \text{Eq. 14}$$

where K_{m^*} is the blood-tissue transfer constant for the trapped metabolite. In general, it will be difficult to mathematically separate the contribution of the trapped metabolite from the parent tracer, and K_x , therefore, cannot be estimated independently of K_{m^*} . However, if only a small amount of metabolite trapping occurs and the flux into the irreversible metabolite

compartment is much less than the flux of the intact tracer into its irreversible compartment, then approximate methods of estimating K_x can be used. If we assume a fixed value for K_m , taken to be in the center of the range of expected values, then K_x can be estimated using the following relationship:

$$\left(\frac{A}{C_{\text{tot}}} - K'_m \cdot \frac{\int C_m \cdot d\tau}{C_{\text{tot}}} \right) = K_x \frac{\int C_x d\tau}{C_{\text{tot}}} + V_{0x} \frac{C_x}{C_{\text{tot}}} + \sum V_{0mi} \frac{C_{mi}}{C_{\text{tot}}} + V_b, \quad \text{Eq. 15}$$

where K'_m is the assumed flux constant for the trapped metabolites. This relationship can be simplified if either Special Case I or Special Case II, described above, applies.

MATERIALS AND METHODS

Tracer and Kinetic Model

To test the performance of the extended graphical estimation method, we applied it to measurement of DNA synthetic rate using the tracer, 2-[^{11}C]thymidine (10,13). Labeled thymidine is incorporated into DNA via the external or salvage pathway; therefore the thymidine incorporation rate (TIR) is a measure of the DNA synthetic rate (10,14–17). The model illustrated in Figure 2 provides a working hypothesis for the behavior of this tracer in proliferating tissues such as tumor or bone marrow (11). We are interested in the flux through the first compartment set representing thymidine transfer to tissue, phosphorylation and incorporation into DNA. Over the time course of the PET experiment, the incorporation of the labeled tracer into DNA is essentially irreversible. The TIR is the flux through this pathway, given by:

$$\text{TIR} = [\text{Tdr}]K_{\text{Tdr}} = [\text{Tdr}] \frac{K_{1t}k_{3t}}{k_{2t} + k_{3t}}, \quad \text{Eq. 16}$$

where $[\text{Tdr}]$ is the blood concentration of native (i.e., unlabeled) thymidine and K_{Tdr} is the blood-tissue transfer constant for the intact tracer (i.e., K_x in the extended graphical analysis formulation). Thymidine labeled in the ring-2 position has two classes of labeled metabolites in the blood (10,16,18): (a) labeled CO_2 and bicarbonate and (b) a group of similar labeled small molecules—thymine, dihydrothymine and β -ureido-isobutyric acid—which is termed the metabolite compartment set. The latter class of metabolites washes out from the tissue and can therefore be modeled as having only an exchangeable tissue compartment. Labeled CO_2 and bicarbonate distribute freely and have largely reversible transport between blood and tissue (18–23). The dashed line in the labeled CO_2 compartment set in Figure 2 indicates the possibility of CO_2 fixation and, thus, irreversible trapping, as has been found in some previous investigations of labeled CO_2 (23,24). Because most of the thymidine degradation takes place in the blood and the liver (16), the compartment sets for intact thymidine and the two classes of metabolites can be modeled as being independent and driven by three separate input functions for most tissues.

A typical set of thymidine and metabolite blood time-activity curves is shown in Figure 3A. The resulting graphical analysis basis functions are shown in Figure 3B, and the graphical plot is shown in Figure 3C. We observed the following:

1. By approximately 15 min after injection, the labeled CO_2 and other metabolites in the blood reach a plateau where the fractional activities of each class of metabolite is nearly constant. Special Case II (simple line fit, Eq. 12) therefore applies to the graphical estimation of K_{Tdr} .
2. Thymidine is rapidly degraded in the blood and has essentially disappeared from the blood within 15 min after injection;

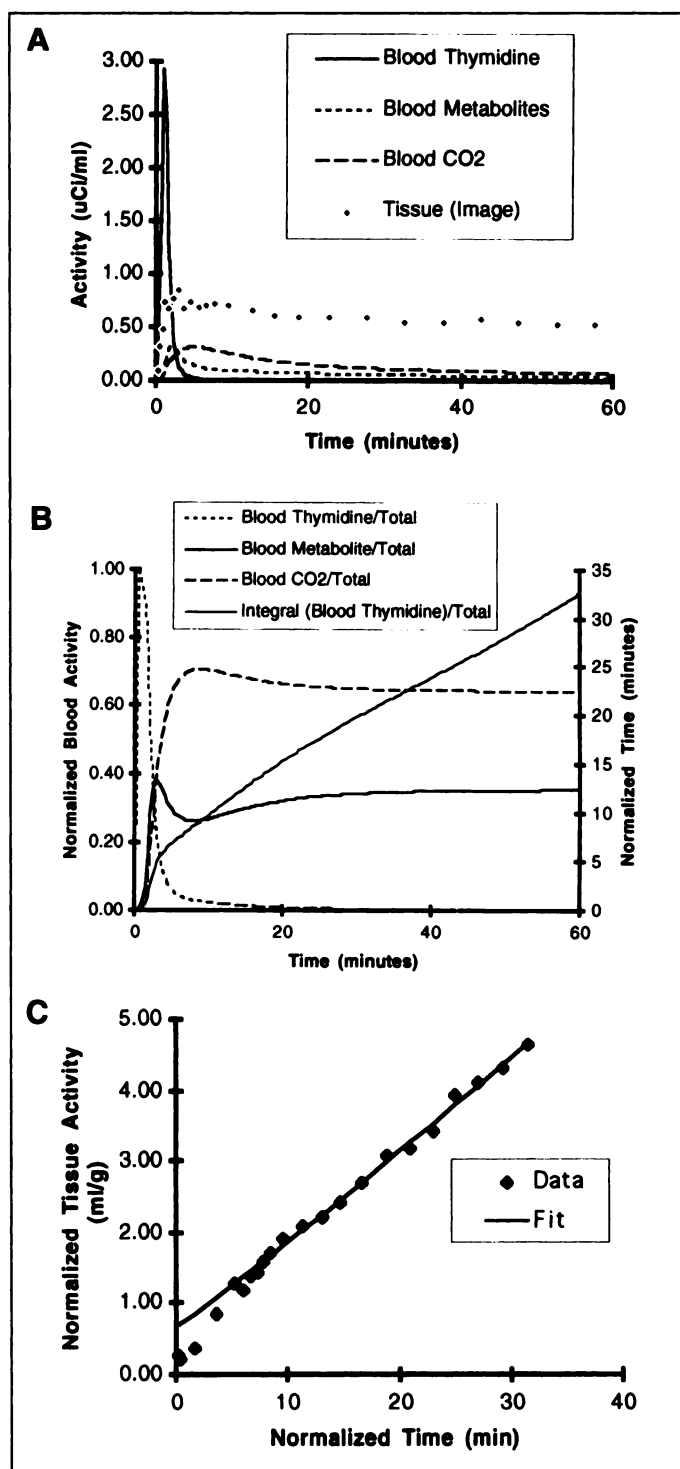


FIGURE 3. Blood and tissue data example from a patient with widely metastatic small-cell cancer of the lung. The tissue time-activity curve is taken from a region of interest placed over a mediastinal node containing active metastatic disease. (A) Raw time-activity curves of tumor (from image), blood thymidine, and blood-labeled metabolites (non- CO_2 metabolites and CO_2). Smoothed blood curves are shown for clarity. (B) Basis functions for graphical analysis. (C) Plot of data and fit for graphical analysis. The plot variables are normalized tissue activity compared with normalized time, as described in Equation 12.

tion; but significant quantities of labeled metabolites are present in the blood throughout the study. The function of the extended graphical analysis method is to separate the contribution of labeled metabolites from the activity of labeled thymidine trapped in DNA.

TABLE 1
Thymidine Model Parameter Ranges and Starting Values

Parameter	Definition	Units	Minimum	Maximum	Starting value
K_{1t}	Thymidine capillary transfer rate constant	ml/min/g	0.050	0.300	0.200
K_{1t}/K_{2t}	Thymidine volume of distribution	ml/g	0.40	4.00	2.25
k_{3t}	Tissue-to-DNA rate constant	1/min	0.000	0.200	0.100
K_{1m}/K_{1t}	Relative metabolite capillary transfer	—	0.80	1.20	1.00*
K_{1m}/K_{2m}	Metabolite volume of distribution	ml/g	0.10	1.00	0.50*
K_{1c}/K_{1t}	Relative CO ₂ capillary transfer	—	0.80	1.20	1.00*
K_{1c}/K_{2c}	CO ₂ Volume of distribution	ml/g	0.20	1.25	0.80
k_{3c}	CO ₂ fixation rate constant	1/min	0.000	0.012	0.005*
V_p	Partial blood volume	ml/g	0.00	0.10	0.05*
Dly	Sampling site to Image site time delay	min	-1	1	0

*Fixed value during compartmental analysis optimization.

Simulations

To test the performance of the extended graphical analysis method, we simulated 2-¹¹C-thymidine. We used blood input functions similar to those shown in Figure 3A to simulate tissue time-activity curves by numerical integration of the model's differential equations (32). Parameter values for the simulations were chosen to represent rate constants for proliferating tissues (11,16,25–31). Where experimental data were not available (e.g., metabolite compartment set), we chose a range for the parameters based on our preliminary experience with the model. Starting values and ranges for each parameter are given in Table 1.

First, noise-free tissue time-activity curves were generated from fixed sets of parameter starting values. These were used to determine the impact of different start and stop times used in the graphical fit of the data, to determine the impact of local metabolism of thymidine in the tissue-of-interest, and to determine the potential impact of labeled CO₂ trapping. In each case the correct answer for the thymidine blood-tissue transfer constant was known from the parameter values used as the input to the simulation. These were used to calculate the true blood-tissue transfer constant (Eq. 4).

To test graphical fit starting and stopping times, we generated a noiseless tissue time-activity curve using the parameter starting values listed in Table 1, with the exception that CO₂ fixation was not allowed ($k_{3c} = 0$). We tested starting times ranging from 5 to 40 min and stopping times ranging from 40 to 60 min, comparing graphically-estimated transfer constants to the true value.

To test the effect of local metabolism of thymidine on the tissue of interest, an additional pathway connecting the tissue thymidine and metabolite compartments (Fig. 2) was added to the model, described by a first order rate constant, k_{met} . A family of noise-free tissue time-activity curves was generated using the parameter starting values in Table 1, with the exception that k_{3c} was set to zero, allowing k_{met} to vary from zero (no local metabolism) to 0.400 min⁻¹, which was four times the value of the tissue-to-DNA rate constant, k_{3t} . For each curve, the graphical estimate was compared to the true blood-tissue transfer constant, in this case given by the following:

$$K_{Tdr} = \frac{K_{1t}k_{3t}}{k_{2t} + k_{3t} + k_{met}} \quad \text{Eq. 17}$$

Compartmental analysis estimates, as described below, were also calculated for comparison.

To assess the effect of a small amount of CO₂ fixation on the estimation of K_{Tdr} , we generated a family of noise-free tissue time-activity curves using the parameter starting values listed in Table 1, this time allowing k_{3c} to vary over its expected range

(0–0.012 min⁻¹), as given in Table 1 (19,20,23,24). This results in a range of 0 to 0.009 ml/min/g for the CO₂ fixation blood-tissue transfer constant, as implied by the assigned values for the other CO₂ rate constants and Equation 4. For each curve, K_{Tdr} was calculated in three ways:

1. Graphical analysis ignoring CO₂ fixation (Eq. 12).
2. Compartmental analysis assuming no CO₂ fixation ($k_{3c} = 0$).
3. Approximate graphical analysis with an assumed CO₂ fixation blood-tissue transfer constant = 0.004 ml/min/g, using Equation 15. This value is at the center of the anticipated range of blood-tissue transfer constants for CO₂ fixation, as implied by the ranges in Table 1.

To test the graphical analysis method under more realistic conditions, tissue time-activity curves were generated allowing all the parameters to vary randomly over the ranges of values in Table 1. This resulted in a range of K_{Tdr} from 0 to 0.22 ml/min/g. CO₂ fixation was simulated by allowing k_{3c} to vary over its expected range, 0 to 0.012 min⁻¹ (19,20,23,24). For comparison, a second set of simulations with no CO₂ fixation ($k_{3c} = 0$) was performed. Poisson noise was added to each point in simulated tissue time-activity curves at a level that would be expected in the typical patient receiving a 555-MBq (15 mCi) injection of [¹¹C]thymidine, a 2 × 2 × 2-cm region of interest in the center of a large tumor, and taking isotope physical decay into account. Under these conditions, the 55–60 min tissue time-activity curve point in the simulated tissue time-activity curve obtained from the parameter starting values in Table 1 would be expected to have an average coefficient of variation of approximately 5%.

In the simulations of tissue time-activity curves with noise, curves were repeatedly generated and analyzed in two ways:

1. Graphical estimation using Equation 15, with an assumed CO₂ fixation blood-tissue transfer constant of 0.004 ml/min/g.
2. Compartmental analysis to estimate the individual rate constants. Previous investigations of simulated data (11) have shown that it is necessary to fix some of the parameters during model optimization to obtain reproducible estimates of the thymidine compartment set rate constants. In this case, the model was optimized by floating K_{1t} , k_{2t} , k_{3t} and k_{2c} . The metabolite and CO₂ K_1 's (K_{1m} and K_{1c}) are assumed to be fixed ratios of K_1 as listed in Table 1. The remaining parameters are fixed to the starting values listed in Table 1, which are close to the centers of their estimated ranges. The thymidine blood-

TABLE 2
Blood-Tissue Transfer Constant Estimation Errors for Various Estimation Start and Stop Times

Start time (min)	Stop time (min)	% Error in graphical estimate
5	60	-9%
10	60	-7%
20	60	-1%
30	60	0%
40	60	0%
20	50	-2%
20	40	-4%

tissue transfer constant, K_{Tdr} , is calculated from the estimated parameters using Equation 4.

For each simulation, 500 tissue time-activity curves were generated, which resulted in reproducible regression analyses for the simulations. Standard error of the estimate/mean values for the regressions of repeated sets of simulations were within 1%–2% of each other.

Patient Data

The graphical analysis method was also applied to the estimation of thymidine blood-tissue transfer constants in patient studies. In these studies, 24-frame dynamic imaging was carried out for 60 min after a 1-min infusion of 185–740 MBq (5–20 mCi) of 2-[^{11}C]-thymidine (33). Imaging was performed on either an Advance Tomograph (GE Medical Systems, Milwaukee, WI) or the UW modified SP3000 scanner (PETT Electronics, St. Louis, MO). After correction for attenuation and scatter, tissue time-activity curves for bone marrow and tumors were obtained from region of interest analysis. Arterial blood samples obtained for 60 min after the start of injection were analyzed for metabolites as described previously (10,18). Blood and tissue time-activity curves were obtained from 10 studies of seven patients. In three patients with tumors, imaging was performed before therapy and after a single administration of chemotherapy. A total of 20 time-activity curves were analyzed, representing data from 16 tumor sites (nine pretherapy; seven post-therapy) and normal marrow in four patients. Each tissue time-activity curve was analyzed both by compartmental analysis and by the extended graphical analysis method. CO_2 fixation rates were assumed to take on fixed values in the noisy-curve simulations as previously described.

RESULTS

Simulations

Table 2 shows the estimated thymidine blood-tissue transfer constant errors using different start and stop times for the fitting process applied to a simulated noise-free tissue time-activity curve representing a tumor with blood-tissue transfer constant equal to 0.106 ml/min/g. Starting times earlier than 20 min resulted in small biases in the estimates of K_{Tdr} . With a 20-min starting time, stopping times greater than 50 min produced biases of less than 2%. For these data, which were simulated without noise, even short fitting intervals provide reasonable estimates. This would not necessarily be the case with noisy data, where longer fitting intervals would likely provide more reliable fits. On the basis of these considerations, starting and stopping times of 20 min and 60 min, respectively, were chosen for graphical analysis in the remainder of the data analysis.

We next used simulated noiseless tissue time-activity curves to test the influence of the local generation of metabolites in the tissue of interest. Figure 4 shows a plot of the estimate compared with true blood-tissue transfer constants. Note that as

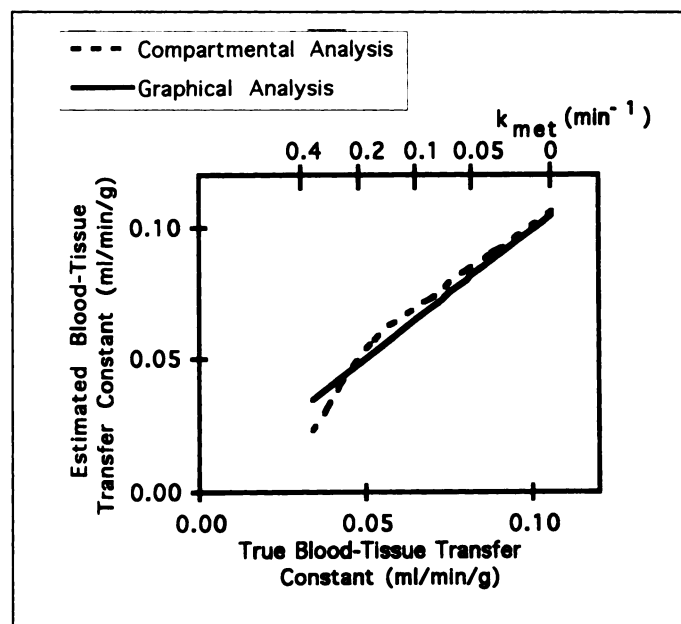


FIGURE 4. Estimated compared with true blood-to-tissue transfer constants for tissue time-activity curves simulated with a variable degree of local tissue metabolism of the tracer. Local metabolism, represented by the parameter k_{met} , is displayed on the top of the graph. Plots for both graphical analysis and compartmental analysis estimates of the blood-tissue transfer constant are shown.

k_{met} increases, the simulated efflux from the reversible tissue thymidine compartment increases, and the resulting blood-tissue transfer constant decreases from a baseline of 0.106 ml/min/g with zero local metabolism to 0.034 ml/min/g with $k_{met} = 0.400 \text{ min}^{-1}$, as described by Equation 17. The graphical estimates remained accurate even at the highest level of local tissue metabolism encountered. At the higher levels of local tissue metabolism, however, the fits of the compartmental model, which assumes no local metabolism, were poor. Parameter estimates reached the limits imposed in the optimization process, and the estimated blood-tissue transfer constant was unreliable.

We also used simulated noise-free tissue time-activity curves to calculate the effect of metabolite trapping due to tissue CO_2 fixation. Figure 5 shows the estimated thymidine blood-tissue transfer constant as a function of the blood-tissue transfer

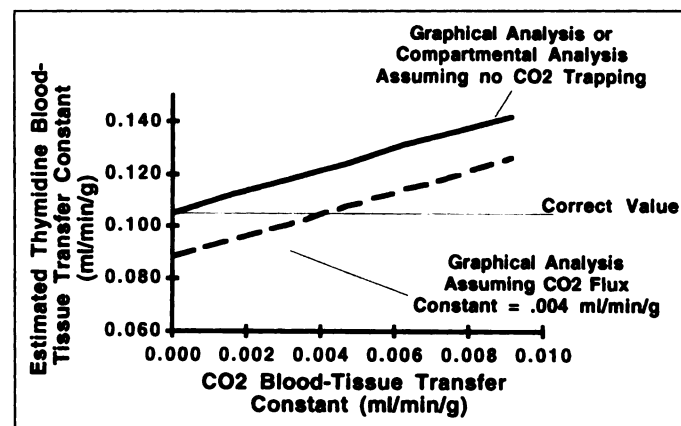


FIGURE 5. Estimated blood-tissue transfer constant estimate compared with CO_2 fixation blood-tissue transfer constant. Plots are shown for graphical estimates and compartmental estimates derived assuming no CO_2 fixation, and the approximate graphical method assuming a transfer constant of 0.004 ml/min/g for CO_2 fixation. The plots for compartmental estimates and graphical estimates assuming no CO_2 fixation are virtually superimposable and appear as a single line at the resolution of this figure.

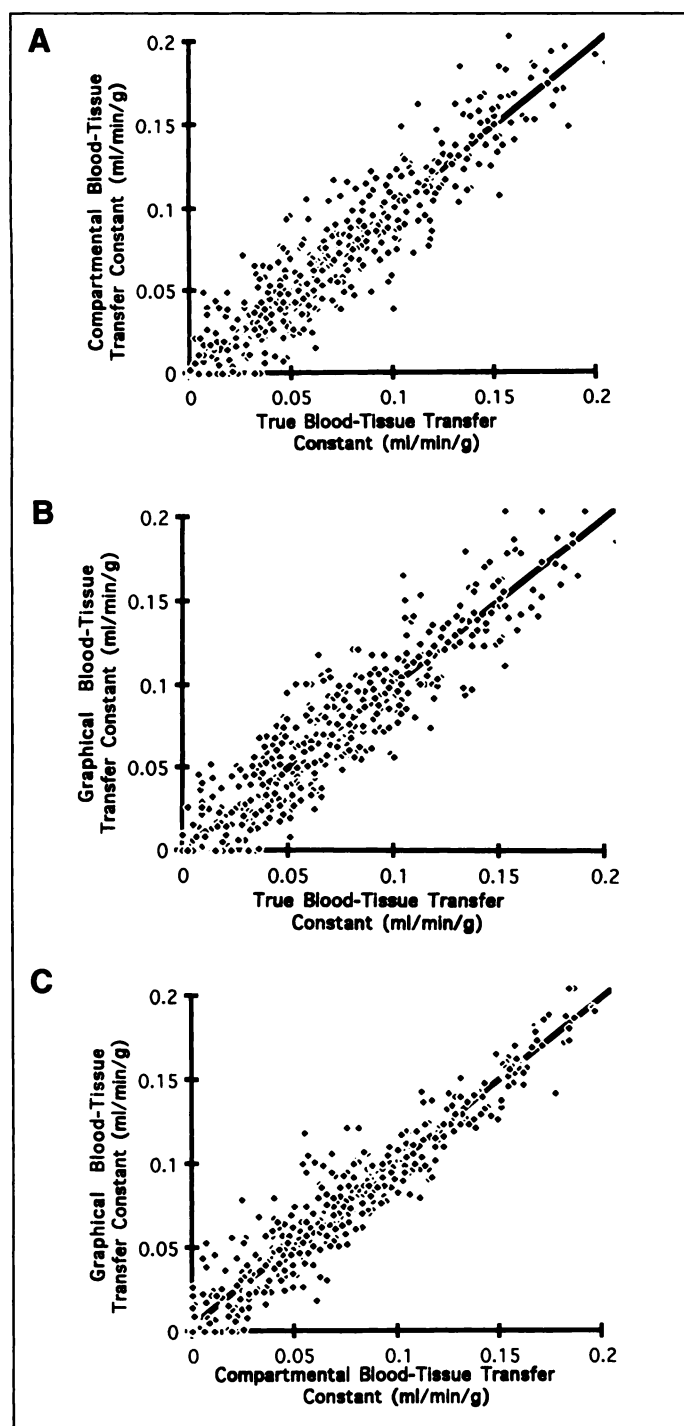


FIGURE 6. Simulation results for noisy data with CO_2 fixation allowed. Regression lines are shown (see Table 3 for regression coefficients). (A) Compartmental estimate compared with true constant. (B) Graphical estimate compared with true constant. (C) Graphical estimate compared with compartmental estimate.

constant for CO_2 fixation. Graphical analysis and compartmental analysis encounter nearly identical errors of up to 30% in the estimates of the thymidine blood-tissue transfer constant as a result of CO_2 fixation. Correcting the graphical estimation process using an assumed CO_2 fixation, blood-tissue transfer constant significantly reduces error for CO_2 fixation rates close to the assumed value, but the method is still prone to error at the extreme values of the expected range.

In the simulations where noise was added and parameters were allowed to vary over their expected ranges, we compared compartmental and graphical estimates compared with true

TABLE 3
Simulation Results

Value	Compartmental vs. true*	Graphical vs. true*	Graphical vs. compartmental†
With CO_2 fixation:			
Slope	0.99	1.00	0.98
Intercept	0.00	0.00	0.00
Correlation (r)	0.932	0.925	0.957
SEE/Mean	23%	25%	19%
No CO_2 fixation:			
Slope	0.99	0.99	0.99
Intercept	0.00	0.00	0.00
Correlation (r)	0.979	0.963	0.975
SEE/Mean‡	12%	16%	13%

*Estimated versus true blood-tissue transfer constants.

†Graphical versus compartmental estimates of blood-tissue transfer constants.

‡Standard error of the estimate divided by the mean.

thymidine blood-tissue transfer constants (Fig. 6A, B). Figure 6C is a plot of the graphical estimate compared with the compartmental estimate. Linear regression values for each of these plots are given in the top portion of Table 3. Regression results for data simulated without CO_2 fixation are also shown in the lower portion of Table 3. Graphical blood-tissue transfer constant estimates that were less than zero were taken to be equal to zero, the limits imposed in compartmental analysis. The graphical method provides estimates of similar accuracy in comparison to compartmental analysis, as judged by the correlation coefficient of the estimated compared with true regressions and the standard errors of the estimate. Comparison of simulations with and without CO_2 fixation demonstrates the increased variability in the estimates that results when one of the metabolites is trapped, even to a small extent. As seen in the graphs, the estimates show the greatest variability at low values of the thymidine blood-tissue transfer constant, where errors in the CO_2 fixation rate should have the largest impact.

Graphical and compartmental estimates of blood-tissue transfer constants for patient studies are plotted against each other in Figure 7. As in the simulations, negative graphical estimates were set to zero. There is reasonable agreement between the estimation methods (slope = 0.88, intercept = 0.00, $r = 0.86$, standard error of the estimate/mean = 43%); however, the correlation between the estimates, as judged by the correlation coefficient and standard error of the estimate, is poorer than in the simulations. The regression slope is less than 1, indicating a tendency for the graphical method to underestimate blood-tissue transfer constants in comparison to compartmental analysis. Because there is no way of knowing the true values, it is difficult to determine whether the graphical estimates, the compartmental estimates, or both are in error.

DISCUSSION

The original papers on the graphical method (1-3) presented a convenient technique for estimating blood-tissue transfer constants for tracers that are irreversibly trapped in tissue. The original formulations required that no labeled metabolites be present outside of the compartment where the tracer is trapped. Patlak et al. (8) formulated an extension of the graphical analysis method where graphical analysis could be applied to systems with labeled metabolites without requiring tissue subtraction measurements. We have extended this method to systems with multiple metabolites under the conditions that the blood concentrations of the metabolites are known and the

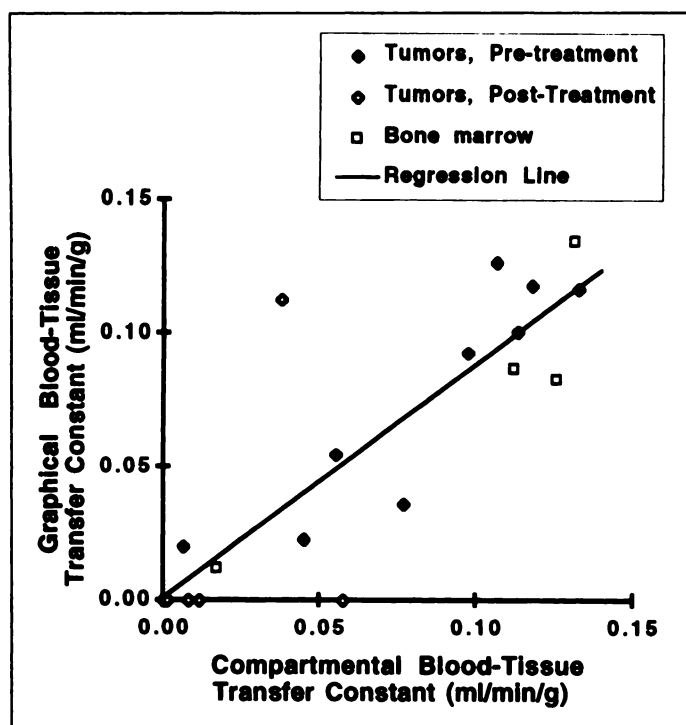


FIGURE 7. Results of patient studies. The graphical blood-tissue transfer constant estimate is plotted compared with the compartmental blood-tissue transfer constant estimate for data obtained from tumor and marrow regions of interest. Regression line is shown. Estimates for several of the post-treatment tumor regions of interest are close to the (0,0) point on the graph and appear as a single point at the resolution of this figure.

metabolites are not irreversibly trapped in the tissue. The result is a graphical estimation problem requiring only linear estimation of, in general, only three or four parameters. This may be handled by techniques such as singular-value decomposition of the design matrix of the estimation equations (34). Under certain conditions, including those encountered in 2-[¹¹C]-thymidine imaging, the estimation problem can be reduced to a simple two-dimensional linear regression, which is the method we used in the analysis of simulated and patient data. We have also presented an approximate estimation method that can be used when one of the metabolites is trapped in tissue to a small extent. This is the approach that was taken for the analysis of both thymidine data simulated with CO₂ fixation and the patient data.

Simulations of 2-[¹¹C]-thymidine have shown that the extended graphical method can accurately estimate blood-tissue transfer constants for tracers with labeled metabolites, and that estimates are comparable to those obtained with compartmental analysis. The simulations showed that as long as the metabolites are not trapped in the tissue of interest, a moderate amount of local metabolism can be tolerated without limiting the accuracy of the estimates of blood-tissue transfer constants for the intact tracer. On the other hand, trapping of the metabolites causes significant errors in the estimates, which can be partially, but not completely, corrected if it is justifiable to assume a fixed value for the blood-tissue transfer constant for metabolite trapping.

On patient data, the graphical estimates of tracer blood-tissue transfer constants agree with compartmental analysis, but with a poorer correlation than predicted by simulations. Because our model is preliminary, we have no validated standard against which to compare the blood-tissue transfer constants estimated from patient data. It is worth noting that the transfer constants we obtained for untreated tumors fall within same range found

by Molnar et al. (35) in their investigation of thymidine uptake in subcutaneously transplanted rat gliomas. Furthermore, in the one instance where there was pathological confirmation of the absence of viable cancer cells in a tumor post-therapy, the graphical method found a blood-tissue transfer rate for thymidine incorporation equal to zero. The accuracy of the graphical estimates of blood-tissue transfer constants for labeled thymidine will need to be assessed as the compartmental model undergoes more rigorous validation through ongoing animal studies.

Further work is necessary to understand the limitations of this method for general application to patient studies. For example, our simulations did not consider noise in the blood measurements. Although blood time-activity curve noise levels are likely to be lower than for the tissue time-activity curves derived from images, even small amounts of noise in these measurements may significantly affect the data since blood activity appears in the denominator of the graphical variables.

Finally, we caution that the extended graphical estimation technique is not a substitute for kinetic modeling, but rather a tool for estimating tracer blood-tissue transfer constants, given an appropriate model for the behavior of the tracer and its labeled metabolites. To be assured that it is appropriate to apply this method, rigorous knowledge of the kinetic behavior of the tracer and metabolites is required. When the method is applicable, it provides a simple technique for calculating the rate of trapping of tracers that would otherwise require complex compartmental analysis. This method therefore makes quantitative imaging of tracers with metabolites a much more tractable task.

CONCLUSION

We have presented a general formulation and preliminary test results of an extension of the Patlak graphical analysis method that applies to systems with labeled metabolites. Our results show that it should be reliable in estimating thymidine incorporation rates for 2-[¹¹C]-thymidine. This method provides a computationally efficient tool for estimating tracer blood-tissue transfer constants for appropriate tracers and may therefore be useful in pixel-wise image analysis.

ACKNOWLEDGMENTS

We thank Dr. Finbarr O'Sullivan and Mark Muzi for helpful discussions, and Suzie Kozawa and Minna Zheng for performing blood sample metabolite analyses. We are indebted to the staff of the University of Washington PET Center for assistance in obtaining the patient studies, in particular Barbara Lewellen and Drs. Thomas Lewellen, Andrew Shields and Daniel Winder. This work was supported in part by National Institutes of Health grants CA39566 and CA42045, the Medical Research Service of the Department of Veterans Affairs and the Mallinckrodt Fellowship of the Society of Nuclear Medicine.

REFERENCES

1. Patlak CS, Blasberg RG, Fenstermacher JD. Graphical evaluation of blood-to-brain transfer constants from multiple-time uptake data. *J Cereb Blood Flow Metab* 1983;3:1-7.
2. Patlak CS, Blasberg RG. Graphical evaluation of blood-to-brain transfer constants from multiple-time uptake data. *Generalizations J Cereb Blood Flow Metab* 1985;5: 584-590.
3. Gjedde A. Calculation of cerebral glucose phosphorylation from brain uptake of glucose analogs in vivo: a re-examination. *Brain Res Rev* 1982;4:237-274.
4. Sokoloff L, Reivich M, Kennedy C, et al. The [¹⁴C]deoxyglucose method for the measurement of local cerebral glucose utilization: theory, procedure and normal values in the conscious and anesthetized albino rat. *J Neurochem* 1977;28:897-916.
5. Phelps ME, Huang SC, Hoffman EJ, et al. Tomographic measurement of local cerebral glucose metabolic rate in humans with [¹⁸F]-2-fluoro-2-deoxy-D-glucose: validation of method. *Ann Neurol* 1979;6:371-388.
6. Reivich M, Alavi A, Wolf A, et al. Glucose metabolic rate kinetic model parameter

- determination in humans: the lumped constant and rate constants for [^{18}F]fluorodeoxyglucose and [^{11}C]deoxyglucose. *J Cereb Blood Flow Metab* 1985;5:179–192.
7. Martin WRW, Palmer MR, Patlak CS, Calne DB. Nigrostriatal function in humans studies with PET. *Ann Neurol* 1989;26:535–542.
 8. Patlak C, Dhawan V, Takikawa S, et al. Estimation of striatal uptake rate constant of FDOPA using PET: methodologic issues. In: Uemura K, Lassen NA, Kanno I, eds. *Quantification of brain function. Tracer kinetics and image analysis in brain PET*. Amsterdam, the Netherlands: Elsevier Science Publishers; 1993:263–268.
 9. Willemsem ATM, van Waarde A, Paans AMJ, et al. In vivo protein synthesis rate determination in primary or recurrent brain tumors using L-[1- ^{11}C]-tyrosine and PET. *J Nucl Med* 1995;36:411–419.
 10. Shields AF, Lim K, Grierson J, et al. Utilization of labeled thymidine in DNA synthesis: studies for PET. *J Nucl Med* 1990;31:337–42.
 11. Mankoff DA, Shields AF, Lee TT, Graham MM. Tracer kinetic model for quantitative imaging of thymidine utilization using [^{11}C]thymidine and PET [Abstract]. *J Nucl Med* 1994;35(suppl):138P.
 12. Huang S-C, Yu D-C, Barrio JR, et al. Kinetics and modeling of L-6-[^{18}F]fluoro-DOPA in human PET studies. *J Cereb Blood Flow Metab* 1991;11:898–913.
 13. Vander Borgh T, Labar D, Pauwels S, Lambotte L. Production of [2- ^{11}C]thymidine for quantification of cellular proliferation with PET. *Appl Radiat Isotopes* 1991;42:103–104.
 14. Vander Borgh T, Lambotte L, Pauwels S, et al. Uptake of thymidine labeled on carbon 2: a potential indicator of liver regeneration by PET. *Hepatology* 1991;12:113–118.
 15. Shields AF, Coonrod DV, Quackenbush RC, Crowley JJ. Cellular sources of thymidine nucleotides: studies for PET. *J Nucl Med* 1987;28:1435–1440.
 16. Cleaver JE. Thymidine metabolism and cell kinetics. *Frontiers Biol* 1967;6:43–100.
 17. Martiat P, Ferrant A, Labar D. In vivo measurement of carbon-11 thymidine uptake in non-Hodgkin's lymphoma using PET. *J Nucl Med* 1988;29:1633–1637.
 18. Shields AF, Graham MM, Kozawa SM, et al. Contribution of labeled carbon dioxide to PET imaging of carbon-11-labeled compounds. *J Nucl Med* 1992;33:581–4.
 19. Brooks DJ, Lammertsma AA, Beaney RP, et al. Measurement of regional cerebral pH in human subjects using continuous inhalation of [^{11}C]-CO $_2$ and PET. *J Cereb Blood Flow Metab* 1984;4:458–465.
 20. Buxton RB, Wechsler LR, Alpert NM, et al. Measurement of brain pH using [^{11}C] CO $_2$ and PET. *J Cereb Blood Flow Metab* 1984;4:8–16.
 21. Hetenyi Jr G, Lussier B, Ferrarotto Jr C. Calculation of the rate of gluconeogenesis from the incorporation of C-14 atoms from labeled bicarbonate or acetate. *Can J Physiol Pharmacol* 1982;60:1603–1609.
 22. Johnson DC, Hoop B, Kazemi H. Movement of CO $_2$ and HCO $_3^-$ from blood to brain. *J Appl Physiol* 1983;54:989–996.
 23. Siesjo BK, Thompson WO. The uptake of inspired [^{14}C]-CO $_2$ into the acid-labile, the acid-soluble, the lipid, the protein and the nucleic acid fractions of rat brain tissue. *Acta Physiol Scand* 1965;64:182–192.
 24. Lockwood AH, Finn RD. [^{11}C]-carbon dioxide fixation and equilibration in rat brain: effects on acid-base measurements. *Neurology* 1982;32:451–454.
 25. Covey JM, Straw JA. Nonlinear pharmacokinetics of thymidine, thymine and fluorouracil and their kinetic interactions in dogs. *Cancer Res* 1983;43:4587–4595.
 26. Goldman D, Bowen D, Gewirtz DA. Some considerations in the experimental approach to distinguishing between membrane transport and intracellular disposition of antineoplastic agents, with specific reference to fluorodeoxyuridine, actinomycin D and methotrexate. *Cancer Treatment Rep* 1981;65:43–56.
 27. Kuebbing D, Werner R. A model for compartmentation of de novo and salvage thymidine nucleotide pools in mammalian cells. *Proc Natl Acad Sci* 1975;72:3333–3336.
 28. Taheri MR, Wickermasinghe RG, Hoffbrand AV. Alternative metabolic fates of thymine nucleotides in human cells. *Biochem J* 1981;194:451–461.
 29. Tew KD, Taylor DM. The relationship of thymidine metabolism to the use of fractional incorporation as a measure of DNA synthesis in tissue proliferation. *Eur J Cancer* 1978;14:153–168.
 30. Wohlhueter RM, Marz R, Plagemann PGW. Thymidine transport in cultured mammalian cells, kinetic analysis, temperature dependence and specificity of the transport system. *Biochim Biophys Acta* 1979;553:262–283.
 31. Yalowich JC, Goldman ID. Analysis of the inhibitory effects of VP-16-213 (etoposide) and podophyllotoxin on thymidine transport and metabolism in Ehrlich ascites tumor cells in vitro. *Cancer Res* 1984;44:984–989.
 32. Graham MM. Parameter optimization programs for PET data analysis. *J Nucl Med* 1992;33:1069.
 33. Courter JH, Link JM, Krohn KA. Automation of the synthesis of [2-carbon-11]thymidine. In: Weinrich R, ed. *Proceedings of the 4th Workshop on Targetry and Target Chemistry*. Villigen, Switzerland: Paul Scherer Institute; 1992:210–214.
 34. Press W, Flannery B, Teukolsky S, Vetterling WT. *Numerical recipes in C*. New York, NY: Cambridge University Press; 1988.
 35. Molnar P, Groothuis D, Blasberg R, et al. Regional thymidine transport and incorporation in experimental brain and subcutaneous tumors. *J Neurochem* 1984;43:421–432.

One-Day Protocol for Cerebral Perfusion Reserve with Acetazolamide

Naoya Hattori, Yoshiharu Yonekura, Fumiko Tanaka, Toru Fujita, Jinyi Wang, Koichi Ishizu, Hidehiko Okazawa, Nagara Tamaki and Junji Konishi

Department of Nuclear Medicine, Kyoto University, Faculty of Medicine, Kyoto; and Biomedical Imaging Research Center, Fukui Medical School, Fukui, Japan

A one-day protocol with a double injection of $^{99\text{m}}\text{Tc}$ -ECD was introduced for the assessment of cerebral perfusion reserve with acetazolamide (ACZ). The purpose of this study was to investigate the feasibility and effectiveness of this protocol. **Methods:** Thirty subjects were given double injections of $^{99\text{m}}\text{Tc}$ -ECD (first dose 370 MBq; second dose 740 MBq) for consecutive brain perfusion studies. Serial dynamic SPECT scans (1 min \times 50 frames) were performed with the first set of SPECT data obtained by totaling the data for the frames taken between 5 and 20 min, and the second by subtracting the decay and dose-corrected initial SPECT data from the sum of the data obtained between 35 and 50 min. To evaluate the feasibility and effectiveness of the procedure, 23 of the 30 subjects were injected with ACZ 14 min after the first dose. To evaluate the reproducibility, seven subjects were not given the ACZ. The washout rate (WR) was calculated for three stages (WR1 = from 6 to 14 min, WR2 = from 20 to 28 min, and WR3 = from 36 to 44 min). Regional count increase (percent increase) and the percent count difference between normal and affected side (percent difference) were also calculated. **Results:** Values for WR1, WR2 and WR3

did not show significant differences among the stages (WR1 = $-1.43\% \pm 6.09\%$, WR2 = $-0.65\% \pm 6.57\%$, and WR3 = $-1.60\% \pm 4.28\%$; F-value = 0.33, p-value = 0.72). Reproducibility was excellent (second SPECT = $0.964 \times$ first SPECT; $r = 0.997$). Mean count increase after ACZ was 21.7%. In patients with unilateral cerebrovascular disease, the percent increase after ACZ loading was significantly greater on the normal side ($26.6\% \pm 13.0\%$) than on the affected side ($19.3\% \pm 13.2\%$) ($p < 0.01$), resulting in a significant increase in percent difference (control: $14.3\% \pm 10.7\%$, ACZ: $19.2\% \pm 11.5\%$; $p < 0.01$). **Conclusion:** ECD washout was minimal during the first 50 min after injection and was not affected by ACZ, which supports the feasibility of this protocol. The simple procedure and short acquisition time of this method renders it clinically useful for measuring cerebral perfusion reserve.

Key Words: acetazolamide; technetium-99m-ECD; double-injection protocol; cerebral perfusion reserve

J Nucl Med 1996; 37:2057–2061

Assessment of cerebral perfusion reserve in patients with an occlusive disease of the major cerebral arteries is important for the evaluation of hemodynamic compromise and candidate selection for revascularization surgery (1–6). Carbon dioxide or

Received Sept. 7, 1995; revision accepted Feb. 9, 1996.

For correspondence or reprints contact: Naoya Hattori, MD, Department of Nuclear Medicine, Kyoto University, Faculty of Medicine, Shogoin, Sakyo, Kyoto, 606 Japan.